



Analysis of Wave Scattering from a Viscoelastic Layer with Complex Shape

Nathalie Favretto-Cristini*

*Aix-Marseille Univ, CNRS, Centrale Marseille
LMA, Marseille, France
favretto@lma.cnrs-mrs.fr*

Arkady M. Aizenberg

*Institute of Petroleum Geology and Geophysics SB RAS
Pr.Ac.Koptyug 3, Novosibirsk 630090, Russia
AizenbergAM@ipgg.sbras.ru*

Bjørn Ursin

*Department of Petroleum Engineering and Applied Geophysics
Norwegian University of Science and Technology
S.P.Andersens vei 15A, Trondheim N-7491, Norway
Centro de Pesquisa em Geofísica e Geologia, Salvador, Bahia, Brazil
National Institute of Science and Technology of Petroleum Geophysics
Instituto de Geociências Universidade
Federal da Bahia Campus Universitário da Federação
Salvador, Bahia, Brazil
bjorn.ursin@ntnu.no*

Paul Cristini

*Aix-Marseille Univ, CNRS, Centrale Marseille
LMA, Marseille, France
cristini@lma.cnrs-mrs.fr*

Anastasiya Tantsereva

*Department of Petroleum Engineering and Applied Geophysics
Norwegian University of Science and Technology
S.P.Andersens vei 15A, Trondheim N-7491, Norway
anastasiya.tantsereva@ntnu.no*

Received 1 July 2016

Accepted 7 February 2017

Published 29 March 2017

The Discretized Kirchhoff Integral method has been recently tested against laboratory experiments using a model with surface curvatures and sharp edges generating wave diffraction effects.

*Corresponding author.

Comparisons between numerical and laboratory data have exhibited a good quantitative fit in terms of time arrivals and amplitudes, except in the vicinity of secondary shadow boundaries created by the interaction of the edges of some topographical structures. Following this work, the effect of multiple scattering and the surface curvatures on the wavefield is studied here, using the so-called diffraction attenuation coefficient, in order to define the cases where these effects may be neglected in the numerical modeling without loss of accuracy.

Keywords: Diffraction; scattering; topography; physical model; numerical modeling.

1. Introduction

Accurate simulation of wave propagation in the presence of complex structures which can generate diffractions is a topic of interest to different scientific domains in acoustics since it is a core tool for imaging and inversion. Among the different numerical methods which can be used in such a context (e.g. ray tracing, finite element method...), methods based on Kirchhoff integral¹ are often preferred because they represent a good trade-off between accuracy and efficiency in terms of computational cost. Recently, the discretized Kirchhoff integral method has been tested against laboratory small-scaled experiments using a physical model with strong 3D topographies and broad-beam sources/receivers.^{2,3} This method is a simplified version of the Tip-Wave Superposition method,⁴ with conventional plane-wave reflection coefficients used instead of the effective reflection coefficients.⁵ It assumes single scattering, i.e. single reflection from interfaces and single diffraction from edges and vertices. The features of the physical model have complicated surface curvatures, several edges and vertices. The comparisons between numerical and laboratory data have exhibited a good quantitative fit in terms of time arrivals and amplitudes, except in the vicinity of secondary shadow boundaries created by the interaction of the edges of some topographical structures. Following our previous work, we now study the effect of multiple scattering and the surface curvature of such complex-shaped structures, in order to define the cases where these effects may be neglected in the numerical modeling without loss of accuracy. Indeed, including both multiple scattering and effective reflection coefficients in the numerical method leads to a significant increase in computational resources and costs. We pay more attention on specific areas of the physical model which generate complicated diffracted wavefields. Besides previous and quantitative analysis,^{2,3} additional insight is provided here through comparisons of the so-called diffraction attenuation coefficient (DAC)^{6,7} evaluated for numerical and laboratory data, and also for approximate solutions taking into account single and double diffractions.

Sections 2 and 3 briefly describe the discretized Kirchhoff integral method and the laboratory experiments, respectively. In Sec. 4, the derivations for the DAC are presented. Wavefields for specific areas are analyzed in Sec. 5, and conclusions are drawn in Sec. 6.

2. Discretized Kirchhoff Integral Modeling

We consider a three-layered medium (Fig. 1). The homogeneous fluid medium \mathbb{D}_1 is characterized by the wave velocity v_{p1} and the mass density ρ_1 . The isotropic viscoelastic medium

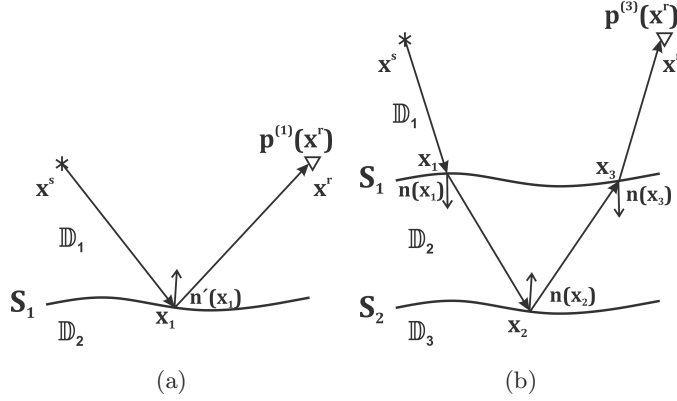


Fig. 1. Schematic representation of the reflections from the top (left) and the bottom (right) of the viscoelastic layer \mathbb{D}_2 .

\mathbb{D}_2 is characterized by the P -wave velocity v_{p2} , the S -wave velocity v_{s2} , the mass density ρ_2 , and the quality factors Q_p and Q_s . The isotropic elastic medium \mathbb{D}_3 is characterized by the P -wave velocity v_{p3} , the S -wave velocity v_{s3} and the mass density ρ_3 . The media are separated by the piecewise smooth interfaces S_1 and S_2 , respectively. Let $\mathbf{x} = (x_1, x_2, x_3)$ be a fixed Cartesian coordinate system. We consider a zero-offset configuration (i.e. the distance between the source and the receiver is zero), with a piezoelectric disk transducer \mathbb{S}_D acting both as a source of incident radiation and as a receiver of reflected and diffracted wavefields.

The scattered wavefield $p(\mathbf{x}^r)$ can be represented as

$$p(\mathbf{x}^r) = p^{(1)}(\mathbf{x}^r) + p^{(3)}(\mathbf{x}^r), \quad (1)$$

where $p^{(1)}(\mathbf{x}^r)$ and $p^{(3)}(\mathbf{x}^r)$ are the reflections from the top and the bottom of the viscoelastic layer \mathbb{D}_2 , respectively. As was shown in Ref. 2, using the Kirchhoff approximation and the far-field approximation, the pressure wavefield at a given receiver point \mathbf{x}^r , singly scattered by S_1 , can be represented by

$$p^{(1)}(\mathbf{x}^r) \approx -\frac{i\omega F(\omega)}{2\pi v_{p1}} \iint_{S_1} (\hat{G}_1(\mathbf{x}^r; \mathbf{x}_1))^2 \cos \theta_{\mathbf{x}_1}(\mathbf{x}_1, \mathbf{x}^r) R_{p_1 p_1}(\theta_{\mathbf{x}_1}(\mathbf{x}_1, \mathbf{x}^r)) dS_1(\mathbf{x}_1), \quad (2)$$

where

$$\hat{G}_1(\mathbf{x}^r; \mathbf{x}_1) \approx \frac{e^{i\omega|\mathbf{x}^r - \mathbf{x}_1|/v_{p1}}}{|\mathbf{x}^r - \mathbf{x}_1|} A[\gamma(\mathbf{x}^r, \mathbf{x}_1)] \quad (3)$$

is the response received at the transducer located at \mathbf{x}^r and emanated from the surface point \mathbf{x}_1 in the far-zone of the transducer. $A[\gamma(\mathbf{x}^r, \mathbf{x}_1)]$ is the directivity function which is the same for both radiation and reception, $\gamma(\mathbf{x}^r, \mathbf{x}_1)$ being the angle between the normal to the transducer's interface and the ray connecting points \mathbf{x}^r and \mathbf{x}_1 . $R_{p_1 p_1}(\theta_{\mathbf{x}_1}(\mathbf{x}_1, \mathbf{x}^r))$ is the plane-wave reflection coefficient of the pressure-pressure type, $\theta_{\mathbf{x}_1}(\mathbf{x}_1, \mathbf{x}^r)$ being the angle between the normal vector $\mathbf{n}'(\mathbf{x}_1)$ at the surface point \mathbf{x}_1 directed into the layer \mathbb{D}_1

and the ray connecting the points \mathbf{x}_1 and \mathbf{x}^r . $F(\omega)$ is the Fourier transform of the source wavelet, ω being the angular frequency.

The wavefield at a given receiver point \mathbf{x}^r , singly scattered by S_2 , is obtained in a similar way as

$$\begin{aligned}
 p^{(3)}(\mathbf{x}^r) &\approx \left(-\frac{i\omega}{2\pi}\right)^3 \frac{F(\omega)}{v_{p1}V_{p2}^2} \iint_{S_1} \hat{G}_1(\mathbf{x}^r; \mathbf{x}_3) \left[\frac{\cos \theta_{\mathbf{x}_3}(\mathbf{x}_3, \mathbf{x}^r) + \cos \theta_T(\mathbf{x}_3)}{2} \right] \\
 &\times \iint_{S_2} T_{\phi_2 p_1}(\theta_{\mathbf{x}_3}(\mathbf{x}_2, \mathbf{x}_3)) G_2(\mathbf{x}_3; \mathbf{x}_2) \left[\frac{\cos \theta_{\mathbf{x}_2}(\mathbf{x}_2, \mathbf{x}_3) + \cos \theta_R(\mathbf{x}_2)}{2} \right] \\
 &\times \iint_{S_1} R_{\phi_2 \phi_2}(\theta_{\mathbf{x}_2}(\mathbf{x}_1, \mathbf{x}_2)) G_2(\mathbf{x}_2; \mathbf{x}_1) \left[\frac{\cos \theta_{\mathbf{x}_1}(\mathbf{x}_1, \mathbf{x}_2) + \cos \theta_T(\mathbf{x}_1)}{2} \right] \\
 &\times T_{p_1 \phi_2}(\theta_{\mathbf{x}_1}(\mathbf{x}^s, \mathbf{x}_1)) \hat{G}_1(\mathbf{x}_1; \mathbf{x}^s) dS_1(\mathbf{x}_1) dS_2(\mathbf{x}_2) dS_1(\mathbf{x}_3), \tag{4}
 \end{aligned}$$

where

$$G_2(\mathbf{x}_k; \mathbf{x}_j) = \frac{e^{i\omega|\mathbf{x}_k - \mathbf{x}_j|/V_{p2}}}{|\mathbf{x}_k - \mathbf{x}_j|} \tag{5}$$

is the Green's function corresponding to the P -wave potential in \mathbb{D}_2 , $|\mathbf{x}_k - \mathbf{x}_j|$ being the distance between the points \mathbf{x}_j and \mathbf{x}_k . The velocity V_{p2} is complex-valued

$$V_{p2} = V_{p2}(\omega) = v_{p2} \left[1 + \frac{1}{\pi Q_p} \ln \left(\frac{\omega}{\omega_r} \right) - \frac{i}{2Q_p} \right], \tag{6}$$

where ω_r is a reference frequency at which the reference attenuation factor $Q_p = Q_p(\omega_r)$ is known and considered as a constant. $\hat{G}_1(\mathbf{x}^r; \mathbf{x}_3)$ and $\hat{G}_1(\mathbf{x}_1; \mathbf{x}^s)$ are given by Eq. (3) with appropriate variables. In Eq. (4), the notation $\theta_{\mathbf{x}_i}(\mathbf{x}_j, \mathbf{x}_k)$ represents an angle between the normal vector at the point (denoted by subscript) and the ray connecting two points (in brackets), whereas the notation $\theta_{R,T}(\mathbf{x}_k)$ represents an angle between the normal vector at the point (shown in brackets) and the wavefields reflected or transmitted (subscript R or T) at the same point. The exact expressions for the frequency-dependent reflection coefficients $R_{p_1 p_1}$ and $R_{\phi_2 \phi_2}$ and transmission coefficients $T_{p_1 \phi_2}$ and $T_{\phi_2 p_1}$ are given in Ref. 8.

3. Laboratory Experiments

A conventional ultrasonic pulse-echo technique has been used to obtain the reflection data from a model containing a full dome, a truncated small dome, a fault, and a truncated pyramid. The model of size 600 mm \times 400 mm \times 70 mm is made of PVC whose viscoelastic properties are in the same range as those of typical geological media. The model has been immersed in a water tank equipped with a computer-controlled system which allows for accurate positioning of the source and receiver. It was placed on a thick aluminum plate for support. The properties of the materials measured within the frequency range [300 kHz–1 MHz] are presented in Table 1. Attenuation in the water and aluminum is negligible.

Table 1. Properties of the materials measured within the frequency range (300 kHz–1 MHz) and associated uncertainties.

| | v_p (m/s) | v_s (m/s) | ρ (kg/m ³) | Q_p | Q_s |
|----------|-------------|-------------|-----------------------------|-------|-------|
| Water | 1476 | — | 1000 | — | — |
| PVC | 2220 ± 10 | 1050 ± 10 | 1412 ± 17 | 40–60 | 27–31 |
| Aluminum | 6440 | 3170 | 2700 | — | — |

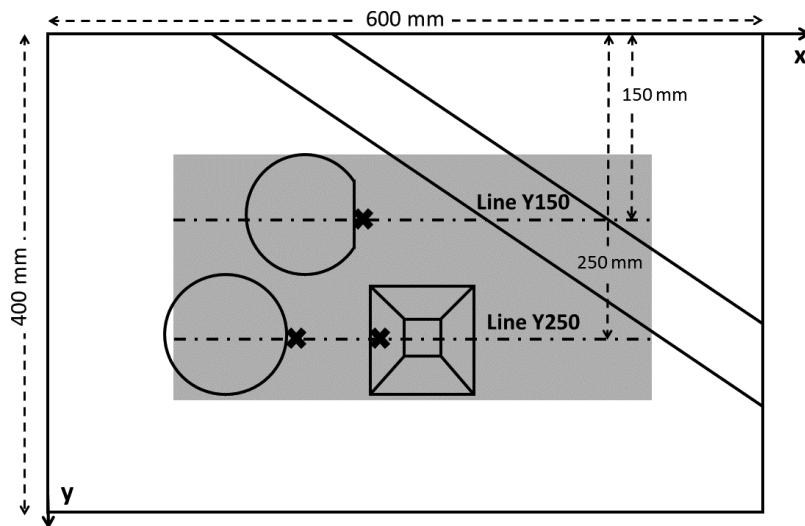


Fig. 2. Acquisition area (light gray) and specific locations (black crosses) considered in this study.

The model has been illuminated using a piezoelectric transducer operating as both a source and a receiver with a dominant frequency equal to 500 kHz. The transducer has a broad-beam aperture (45° at -3 dB). We have considered a scaling factor $\mu = 2.10^4$: the experimental frequency of 500 kHz corresponds to a real frequency of 25 Hz, and the experimental distance of 10 mm to a real distance of 200 m, velocities as well as densities and attenuations remain unchanged. A more detailed description of the experimental setup and conditions can be found in Ref. 2. Acquisitions have been performed along Y-lines with a spatial sampling Δx equal to 2 mm (Fig. 2).

4. Edge Diffraction Modeling

The wavefield in the presence of diffracting features has been widely studied within the framework of the geometrical theory of diffraction. However, this theory breaks down, for instance, in the vicinity of the shadow boundaries,⁷ often referred to as boundary layers. To overcome this difficulty, a better description of the diffraction phenomenon in such neighborhoods has been then proposed by Klem-Musatov.⁷ Within the theory of edge and tip diffraction for singly-scattered wavefields, he introduced a special complex-valued function

$W(u)$, that is related to the generalized Fresnel integral,

$$W(u) = \frac{1}{\pi} \int_0^\infty \frac{u}{u^2 + \xi^2} e^{\frac{i\pi\xi^2}{2}} d\xi \quad (7)$$

for compensating for the discontinuity in amplitude of the reflected wave propagating from a semi-infinite face at the shadow boundary caused by the edge of the face. The parameter $u = \sqrt{4f(\tau_d - \tau_g)}$, that is a derivative of the Fresnel zone size,⁹ indicates the distance from the shadow boundary. Here, f is the dominant linear frequency, τ_d and τ_g are the two-way traveltimes corresponding to the diffracted and geometrical (reflected) waves, respectively. The amplitude of the wavefield in the boundary layer is thus equal to

$$A(u) = \begin{cases} A_g W(u) e^{i\omega\tau_d} & \text{in the shadow zone,} \\ A_g (e^{i\omega\tau_g} - W(u) e^{i\omega\tau_d}) & \text{in the illuminated zone,} \end{cases} \quad (8)$$

where A_g is the amplitude of the geometrical wavefield.

The so-called diffraction attenuation coefficient (DAC) is often used in order to analyze the wave structure of the seismograms recorded in environments with diffracting structures.⁶ Here, this coefficient helps essentially in evaluating the efficiency of accounting for diffractions effects in numerical modeling. We introduce the DAC for singly-scattered wavefields (i.e. $\text{DAC}_{\text{app,ss}}$) as the absolute value of the ratio of the wavefield amplitude A described by Eq. (8) and the amplitude of the geometrical wave A_g . The DAC evaluated from the numerical seismograms obtained with the discretized Kirchhoff integral method (i.e. DAC_{num}) accounts for single scattering only, which is sufficient for most of the offsets. Nevertheless, for some problematic offsets discussed below, considering multiple scattering may be needed. We refer the reader to^{6,10,11} for more details on the evaluation of the DACs, and more specifically on the approximate evaluation of the DAC for doubly-scattered wavefields (i.e. $\text{DAC}_{\text{app,ds}}$).

5. Comparisons and Wavefield Analysis

In this section, we study the wavefield in the presence of diffracting edges. We pay more attention to specific locations along the lines Y150 and Y250, marked with black crosses in Fig. 2. They cover wedge shapes at the sides of the truncated pyramid, the full dome, as well as the truncated part of the small dome. Besides reflections from the flat and spherical parts of the model, they contain diffracted wavefields generated by edges. Quantitative analysis between numerical and experimental data is provided through comparisons of DAC evaluated for numerical (DAC_{num}) and laboratory (DAC_{lab}) data, and for approximate ($\text{DAC}_{\text{app,ss}}$ and $\text{DAC}_{\text{app,ds}}$) solutions. The results for the problematic offsets are presented in Figs. 3–7 and in Table 2.

Consider the vicinity of the truncated pyramid, and more specifically a trace in the shadow zone of the left edge of the lower flat face (Fig. 2). The trace is composed of several groups of reflected and diffracted wavefields generated, for instance, from the edge of the lower flat face (denoted by $T1$ in Fig. 3(a)), from the left edge of the upper flat face ($T2$),

Table 2. Diffraction attenuation coefficient (DAC) evaluated for approximate ($\text{DAC}_{\text{app,ss}}$ and $\text{DAC}_{\text{app,ds}}$) solution, numerical (DAC_{num}) and laboratory (DAC_{lab}) data. Relative discrepancies between DAC_{lab} and $\text{DAC}_{\text{app,ss}}$, $\text{DAC}_{\text{app,ds}}$, and DAC_{num} , respectively, are indicated in brackets.

| | Approximate Solutions | | Numerical Data | Laboratory Data |
|----------------------|------------------------|------------------------|-------------------------|-----------------|
| | Single Scattering | Double Scattering | | |
| Truncated pyramid | 0.466 ($\sim 1.5\%$) | 0.450 ($\sim 5.0\%$) | 0.450 ($\sim 5\%$) | 0.473 |
| Full dome | 0.500 ($\sim 13\%$) | 0.428 ($\sim 3.5\%$) | 0.501 ($\sim 13\%$) | 0.443 |
| Truncated dome (cut) | 0.580 ($\sim 36\%$) | 0.424 ($< 1\%$) | 0.535 ($\sim 25.5\%$) | 0.426 |

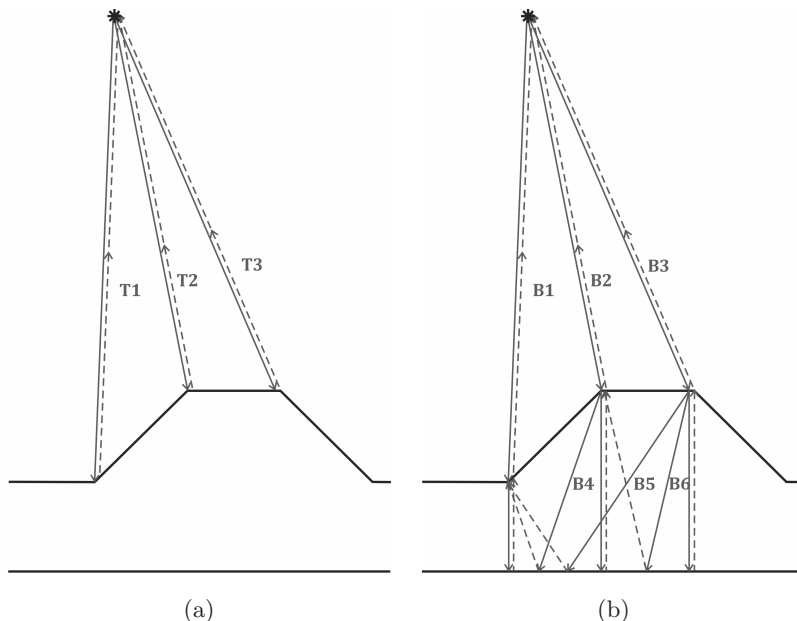


Fig. 3. Schematic representation of the singly-scattered wavefields from the left-hand side of the truncated pyramid (line Y250) for (a) the top of the PVC layer and (b) the bottom of the PVC layer.

or from the right edge of the upper flat face ($T3$), as well as from the bottom of the viscoelastic medium ($B1$ – $B6$ in Fig. 3(b)). All the groups of waves are quite well separated in time. Qualitative comparison of laboratory and numerical traces shows a good fit both in amplitude and traveltime (Fig. 4). Quantitative comparison through the evaluation of the DACs shows that $\text{DAC}_{\text{app,ss}}$ is very close to DAC_{lab} , and much closer than $\text{DAC}_{\text{app,ds}}$ (Table 2). Consequently, taking into account single scattering only is sufficient to describe the wavefield behavior in terms of amplitude in the vicinity of the truncated pyramid, since double diffraction does not play any significant role in this case. However, DAC_{num} approximates DAC_{lab} with a relative discrepancy of 5%. It seems that the discontinuity in the slope of the pyramid has an impact on the wavefield.

Consider now the vicinity of the full dome, and more specifically a trace close to the edge at the right-hand side (Fig. 2). The trace is composed of several groups. The first

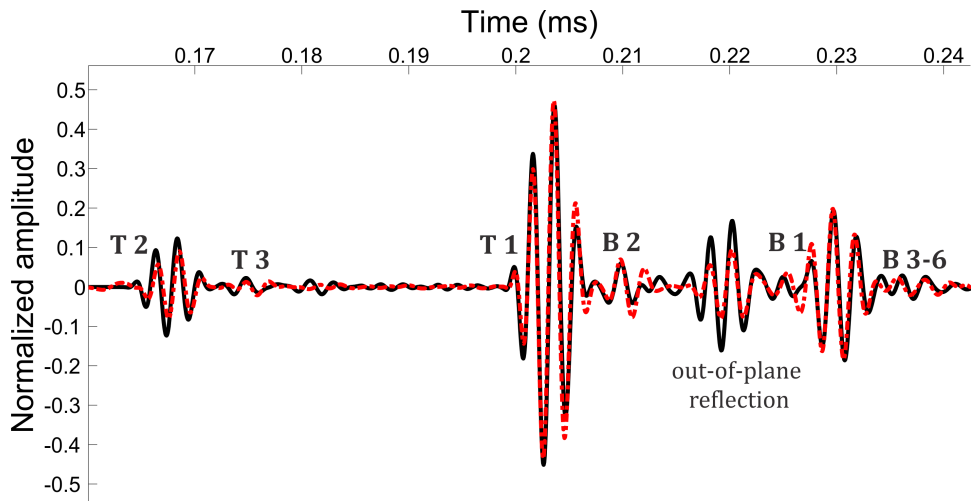


Fig. 4. (Color online) Comparison of the laboratory (red dash-dotted line) and numerical (black solid line) traces located at the left-hand side of the truncated pyramid (line Y250).

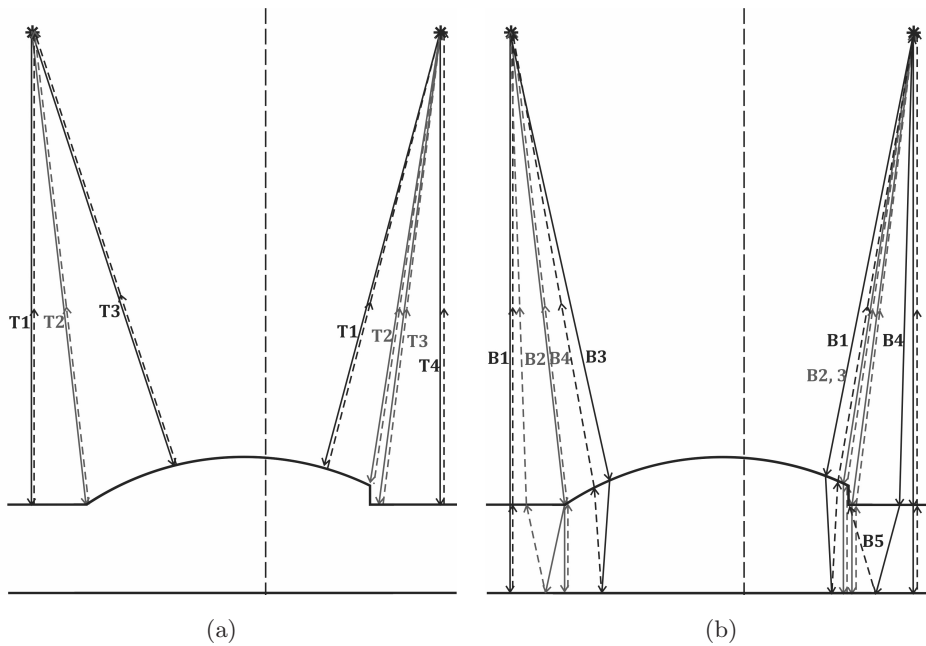


Fig. 5. Schematic representation of the singly-scattered wavefields from the front and the cut of the small dome (line Y150) for (a) the top of the PVC layer and (b) the bottom of the PVC layer.

one corresponds to the wavefield reflected from the dome ($T3$ in Fig. 5(a), left-hand side), well separated in time from the rest of the wavefields. The second group corresponds to the reflection from the flat face ($T1$) and the diffractions from the edge of the flat face and the dome ($T2$), whose traveltimes almost coincide. The third group is composed of the reflections

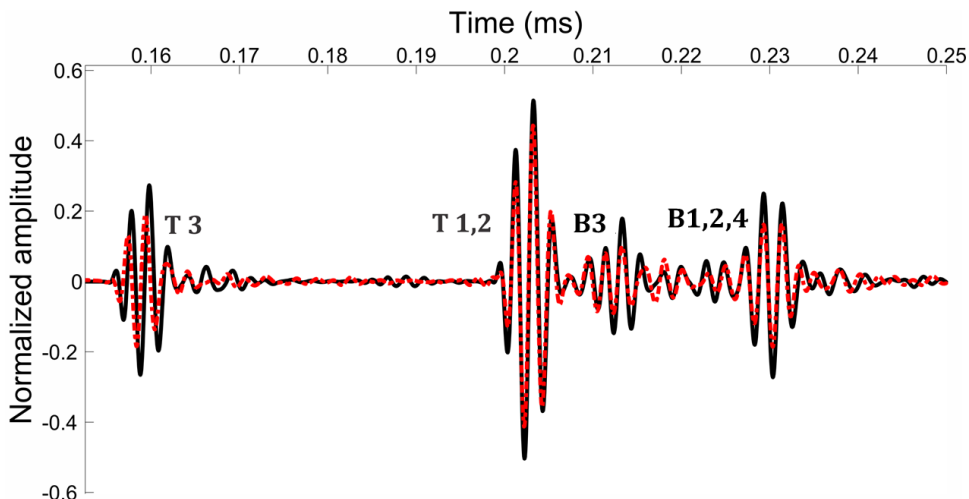


Fig. 6. (Color online) Comparison of the laboratory (red dash-dotted line) and numerical (black solid line) traces located at the right-hand side of the full dome (line Y250).

from the bottom of the viscoelastic medium ($B1$ – $B3$), whereas the fourth one is composed of two waves doubly diffracted from the edge of the flat face and the edge of the dome ($B2$ – $B4$). The laboratory data and numerical traces exhibit a good fit both in amplitude and traveltime for the events (Fig. 6), except for $B2$ – $B4$. Quantitative comparison through the evaluation of the DACs (Table 2) confirms the importance of taking into account double scattering in modeling. Indeed, DAC_{num} is significantly higher than $DAC_{app,ds}$ that best approximates DAC_{lab} , with a relative discrepancy equal to 3.5%. Moreover, the high value of DAC_{num} , together with the small misfit in time and amplitude of the event $T3$, suggests an effect of the edge curvature that must be taken into account in a more appropriate way in the modeling code. Similar observations can be made for the case of the small truncated dome, the only difference between the full and the small dome being the surface curvature.

Finally, consider the vicinity of the truncated part of the small dome, and more specifically a trace in the illuminated zone of the lower edge of the truncated dome (Fig. 2). The trace is composed of the reflected wavefields from the dome ($T1$ in Fig. 5(a), right-hand side) and from the flat face ($T4$), the diffracted wavefields from the upper edge ($T2$) and from the lower edge ($T3$), as well as the reflected wavefields from the bottom of the viscoelastic medium and the doubly-scattered wavefields ($B1$ – $B5$). The wavefields $T1$ – $T4$ are well separated in time. The traveltime for the doubly-scattered wavefield almost coincides with the traveltime for the wavefields $T3$ – $T4$. Qualitative comparison between the laboratory data and numerical traces exhibits acceptable fit both in amplitude and traveltime between the wavefields reflected and diffracted by the top of the medium, but noticeable discrepancies for the wavefields scattered by the bottom (Fig. 7). Moreover, DAC_{num} approximates DAC_{lab} with a high relative discrepancy of about 26% (Table 2). Although this value is better than for the $DAC_{app,ss}$ (relative discrepancy of 36%), it is much worse than that provided by

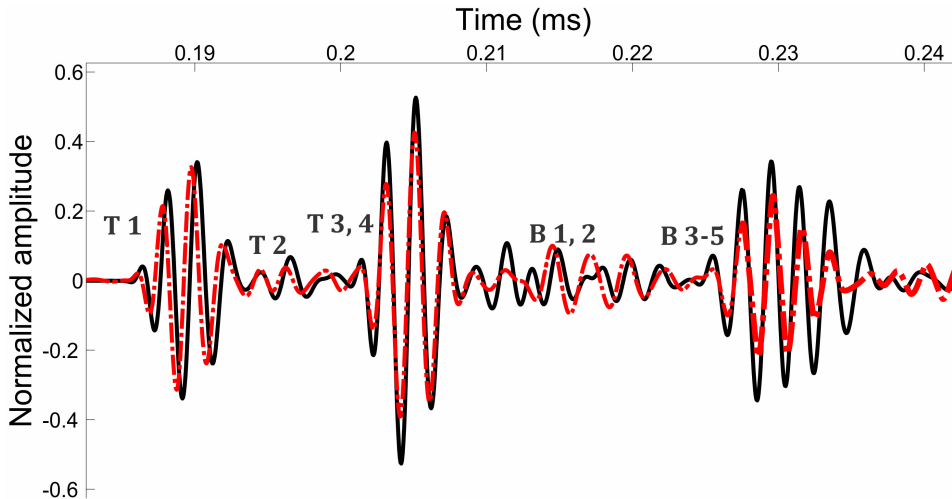


Fig. 7. (Color online) Comparison of the laboratory (red dash-dotted line) and numerical (black solid line) traces located at the cut of the small dome (line Y150).

$\text{DAC}_{\text{app,ds}}$ (relative discrepancy less than 1%). These results strongly suggest that, in the vicinity of the truncated part of the small dome, double scattering is predominant and must be taken into account into modeling. The effect of the edge curvature seems negligible in this case.

From Table 2, we can also note that, from the truncated pyramid to the full dome and then to the truncated dome case, the relative discrepancies between the numerical and laboratory data increase from 5% to 25.5%. This trend is similar to that observed for the approximate solution based on single scattering, and opposite to that observed for the approximate solution based on double scattering. This is fully consistent with one of the underlying assumptions (single scattering) of the numerical method used. These trends show that the double-scattering effect becomes more and more predominant and complex with increasing complexity in the shape of the topographical structures, in particular for structures with sharp edges characterized by angles close to $\frac{\pi}{2}$. As a consequence, the double-scattering effect must be taken into account in the numerical method for simulating the complex wavefields more accurately.

6. Conclusion

The discretized Kirchhoff integral method uses plane-wave reflection coefficients and assumes single scattering. Recent tests against laboratory experiments using a model with surface curvatures and sharp edges generating wave diffraction effects have shown that this method can reproduce correctly the wavefields, except in the vicinity of secondary shadow boundaries created by the interaction of the edges of some topographical structures. Following this work, we have studied here the effect of multiple scattering and the surface curvatures on the wavefield, in order to define the cases where these effects may be neglected

in the numerical modeling without loss of accuracy. Quantitative analysis has been conducted through comparisons of the so-called diffraction attenuation coefficient evaluated for numerical and laboratory data, and also for approximate solutions taking into account single and double diffractions. Surprisingly, replacing the plane-wave reflection coefficient by the effective reflection coefficient in the presence of most of the topographical structures is not mandatory, in particular if a trade-off between accuracy and low computational costs is sought. On the contrary, it has been shown that double scattering is predominant for most of the topographical structures, in particular for structures with sharp edges characterized by angles close to $\frac{\pi}{2}$. Therefore, double scattering must be included in the numerical method, in order to obtain a much better modeling of wavefields.

A modified version of the TWSM that evaluates multiply-scattered wavefields is currently developed and tested. Besides the mathematical derivations that are a bit tricky (e.g. modification of the cascade diffraction terms, correct and stable approximation of the propagation matrix and the diffraction integral operators), including double scattering in the method requires to decrease by 16 (at least) the area of the curved triangles that mesh the interface, and then leads to a drastic decrease in the speed of evaluation in comparison to the simplified version of TWSM used in this paper. Fortunately, using a GPU cluster will permit to reach a reasonable cost in terms of computational time at the end.

Acknowledgments

BU has received financial support from Statoil-Brazil and CNPq-Brazil through the project No. 400757/2014-1, and from the Norwegian Research Council through the ROSE project. The Institute for Engineering and Systems Sciences (INSIS) of the French National Center for Scientific Research (CNRS) is greatly acknowledged for financial support through the PICS BENCHIE project. The authors would like to thank two anonymous reviewers for their constructive comments.

References

1. Y.-H. Pao and V. Varatharajulu, Huygens' principle, radiation conditions, and integral formulas for the scattering of elastic waves, *J. Acous. Soc. Am.* **59** (1976) 1361–1371.
2. A. Tantsereva, B. Ursin, N. Favretto-Cristini, P. Cristini and A. M. Aizenberg, Numerical modeling of 3D zero-offset laboratory data by a discretized Kirchhoff integral method, *Geophysics* **79**(2) (2014) T77–T90.
3. A. Tantsereva, B. Ursin, N. Favretto-Cristini, P. Cristini and A. M. Aizenberg, Errata to “numerical modeling of 3D zero-offset laboratory data by a discretized Kirchhoff integral method”, *Geophysics* **79**(5) (2014) Y3–Y4.
4. M. A. Ayzenberg, A. M. Aizenberg, H. B. Helle, K. D. Klem-Musatov, J. Pajchel and B. Ursin, 3D diffraction modeling of singly scattered acoustic wavefields based on the combination of surface integral propagators and transmission operators, *Geophysics* **72**(5) (2007) SM19–SM34.
5. M. A. Ayzenberg, I. Tsvankin, A. M. Aizenberg and B. Ursin, Effective reflection coefficients for curved interfaces in transversely isotropic media, *Geophysics* **74**(5) (2009) WB33–WB53.

6. A. A. Ayzenberg, Transmission-propagation operator theory and tip-wave superposition method for sub-salt shadow wavefield description, PhD thesis, Norwegian University of Science and Technology (2015).
7. K. D. Klem-Musatov, *Theory of Seismic Diffractions* (SEG, 1994).
8. L. T. Ikelle and L. Amundsen, *Introduction to Petroleum Seismology* (SEG, 2005).
9. N. Favretto-Cristini, P. Cristini and E. de Bazelaire, What is a seismic reflector like? *Geophysics* **74**(1) (2009) T13–T23.
10. A. M. Aizenberg, A system of irregular fundamental solutions to wave equation in a three-dimensional inhomogeneous medium, *Russ. Geol. Geophys.* **34**(4) (1993) 105–113.
11. D. S. Jones, Double knife-edge diffraction and ray theory, *Q. J. Mech. Appl. Math.* **26**(1) (1973) 1–18.